ENHANCED STABILITY INVESTIGATION OF HIGH-GAIN BOOST CONVERTER FOR PHOTOVOLTAIC SYSTEM

S. SANGEETHA¹, R. RAMAPRABHA²

Keywords: PV module; High gain converter (HGC); Electromagnetic compatibility (EMC); Maximum power point tracking (MPPT); MATLAB.

An effective DC-DC converter is recommended for use in renewable energy applications, as suggested in the study. For the design of a high-gain boost converter (HGC), switched inductor cells (SIC) and voltage multiplier cells (VMC) are utilized. VMC provides high voltage gain in the converter side, while switched inductor cells provide a constant source current. Efficiency enables the recommended converter to maintain a high voltage gain at a low duty ratio. The converter stability is achieved under state space modelling (SSM). The electromagnetic compatibility (EMC) condition of the power converter is verified using a spectrum analyzer. The power semiconductor's electrical discharge and potential energy under steady-state conditions, the Bode plot, and the Nyquist plot are examined. Furthermore, the interface of the PV module with a high-gain converter is simulated for the specified values.

1. INTRODUCTION

A high-gain boost converter is a type of DC-DC converter designed to increase the input voltage to a much higher level while ensuring high efficiency. These converters are becoming increasingly significant in applications where effective power conversion is crucial, such as photovoltaic (PV) systems, electric vehicles (EVs), and uninterruptible power supplies (UPS). In particular, the rising demand for renewable energy sources, high power density, and energyefficient solutions has led to a growing reliance on high-gain boost converters to meet these needs. In this work, the converter topology has been selected in accordance with the system requirements. The selection criteria encompass switching methods, power flow directions, isolation type, supplied voltage, and system stability.

The voltage gain in high-gain boost converters has been increased in [1, 2] by utilizing passive switching capacitors. However, as the gain on the capacitor side rises, it leads to higher ripple current on the source side, potentially affecting efficiency and stability. The interleaved configuration of boost converters, as described in [3,4], has been utilized with multiple boost converters featuring offset switching phases to minimize output voltage ripple. This configuration improved efficiency by distributing the load across numerous converters, thereby lowering the stress on individual components. In [5], a review of some commonly used techniques for extending gain was presented. Voltage spikes across the switches are caused by increased leakage inductance, which results from raising the turns ratio. Although clamp circuits [6–8] were used to reduce the spikes, these converters still did not individually meet the grid voltage requirements. Therefore, further extension techniques are necessary to achieve an optimal voltage conversion ratio. In [9], a thorough analysis of non-isolated switched boost converters is provided. The converters are categorized into five primary groups, each of which is carefully investigated: isolation, power flow direction, input port feeding type, soft switching capability, and the presence of right-half-plane zero. In [10], the gain increase was achieved using a voltage multiplier system. An active switching inductor boost converter was also employed in high-gain topologies. A steady input current, low voltage rating for the passive resistance, and minimal voltage stress across the diode characterize the circuit in [11,12]. As demonstrated in [13], the high-efficiency boost converter can

In this work, high-gain operation is achieved by combining a three-diode gain cell with two symmetric voltage multiplier cells. From the results, it is observed that the converter provides a voltage gain of 8 with a symmetrical structure and yields a stable output.

Followed by this introduction section, the overview of the work is described in section 2. The modeling of PV has been achieved for the system's input power requirements and is presented in section 3. The HGC and system stability are discussed in sections 4 and 5, while the simulation results are found in section 6. Electromagnetic compatibility (EMC) is crucial in the design of high-gain boost converters to ensure efficient operation while minimizing electromagnetic interference (EMI) in sensitive applications, as discussed in section 7.

2. SCHEMATIC REPRESENTATION OF HGC

HGC diagrammatic representation is presented in Fig. 1.

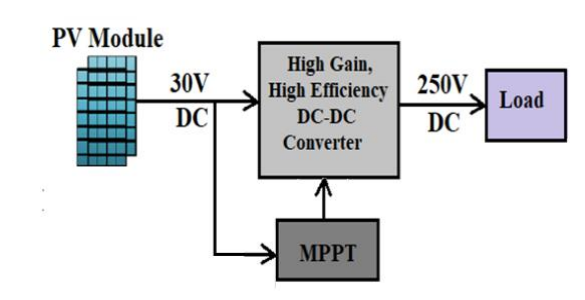


Fig. 1 – Diagrammatic illustration of the system.

A photovoltaic (PV) module is designed to produce approximately 250 W of power. It is then stepped up through a boost converter, after which the power is tracked using a maximum power point tracking (MPPT) technique. In recent decades, PV has played a significant role among researchers. Nonlinear characteristics of the PV system are represented by the I-V and P-V curves. The Maximum power will be affected by temperature and irradiance. PV arrays require maximum power point tracking (MPPT) systems due to their low conversion efficiency. The impulsive standard algorithm

step up the voltage by using its various components. In [14], a non-isolated bidirectional DC-DC converter topology was proposed to improve efficiency and reduce cost. The HGC presented throughout this study is to address these drawbacks. Moreover, the suitability of this HGC for PV interfacing is also discussed.

¹ Sri Sivasubramaniya Nadar College of Engineering, Kalavakkam, Tamil Nadu 603110, India. Email: sangeetha15014@eee.ssn.edu.in, ramaprabhar@ssn.edu.in

known as MPPT modifies the power link to optimize the energy harvesting in the face of moment-to-moment variations in temperature, light intensity, shade, and photovoltaic module characteristics. Under varying atmospheric conditions, the MPPT's job is to modify the solar operating voltage in the vicinity of the MPP. The INC method, also known as the perturb and observe (P&O) method, plays a significant role in the MPPT technique.

3. PV MODELLING AND ITS SPECIFICATIONS

PV systems come with the necessary subsystems to convert solar energy into electrical energy suitable for specific types of loads. There are two primary ways in which the sun provides energy to humans. Heat is used in one case, while light is used in the other. With larger area cells, the solar cell used in this converter can produce up to 250 W and 8.5 A in addition to 30 V of voltage.

Equation (1) represents the PV array's output voltage, which is derived from [15] and can be used to interpret the array's output current.

$$I = I_{ph} \left[\exp\left(\left(\frac{q(V + IR_s)}{KT_C} \right) - 1 \right) \right] - \left(\frac{V + IR_s}{R_P} \right) \tag{1}$$

Parameters of solar PV module from datasheet are specified in Table 1.

Table 1
Parameters of Solar PV Module

Datasheet Parameters	Specifications
$\label{eq:max} \begin{split} & \text{Maximum power } (P_{\text{max}}) \\ & \text{Maximum power voltage } (V_{\text{mp}}) \\ & \text{Maximum power current } (I_{\text{mp}}) \end{split}$	250 W
Maximum power voltage (V _{mp})	31.5 V
Maximum power current (I _{mp})	7.94 A
$ m V_{oc}$	37.8 V
I_{sc}	8.7 A

The I-V and P-V characteristics of the PV array are depicted in Fig. 2.

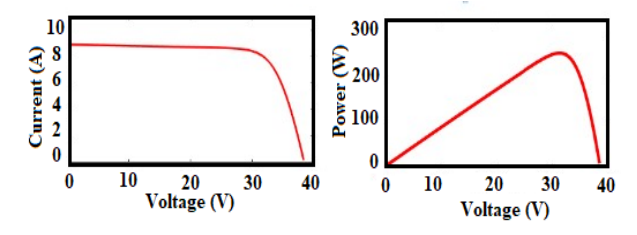


Fig. 2 - Characteristics of PV array.

4. INVESTIGATION OF HGC

The boost converter, with high efficiency, boosts the voltage from 30 V to 250 V through its components, which include two switches, seven diodes, five capacitors, and four inductors. A 90% efficiency is achieved for this converter topology. Two different modes of operation are conducted under forward and reverse bias conditions. By applying KVL and KCL, the mathematical equations are derived for both modes. Two identical switches have been used in this topology to increase the converter gain. The converter consists of seven diodes (D_1 to D_7), two switches (S_1 and S_2), five capacitors (C_1 to C_5), and four inductors (L_1 to L_4). The switches S_1 and S_2 turn on and off simultaneously with the same gating pulse.

Based on the switching waveforms, this system operates in two modes. The schematic representation of HGC is presented in Fig. 3. The switching waveforms of HGC are represented in Fig. 4.

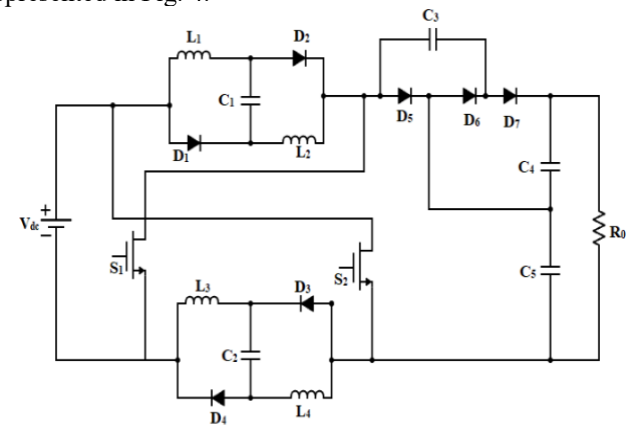
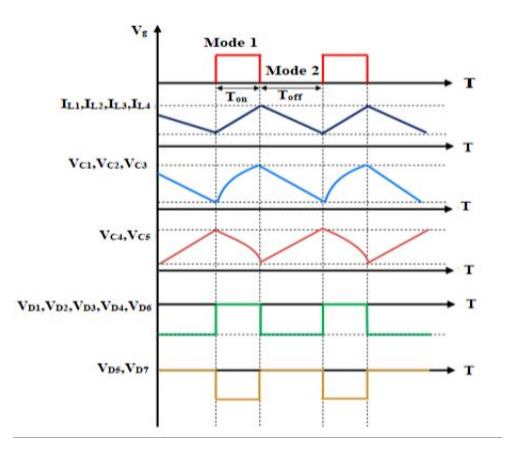


Fig. 3 – Schematic representation of the converter.



 $Fig.\ 4-Switching\ waveforms\ of\ HGC.$

During the T_{on} condition, diodes D_1 and D_6 , as well as switches S_1 and S_2 , are forward-biased. In contrast, diodes D_5 and D_7 are in reverse bias condition. Additionally, the capacitors C_4 , C_5 , and other capacitors are discharging while capacitors C_1 , C_2 , and C_3 are charging. Equations (2) to (9) represent the voltage and current expressions of the inductor and capacitor, derived by applying KVL & KCL in mode 1, as shown in Fig. 5.

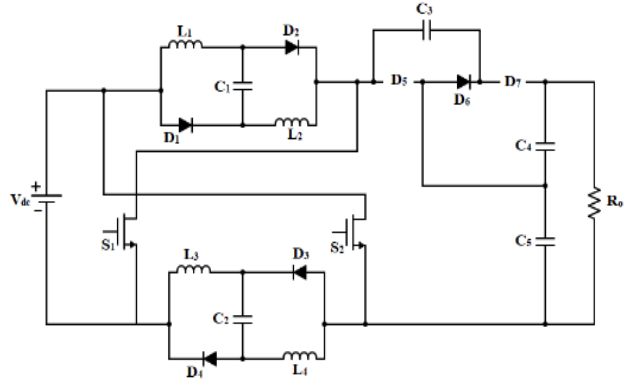


Fig. 5 – First mode of operation.

By applying KVL and KCL, the equations derived under mode one condition are specified in eq.(2-9), by KVL,

$$V_{L1} = V_{L2} = V_{L3} = V_{L4} = V_{in}$$
 (2)

$$V_{in} = V_{C1} = V_{C2} \tag{3}$$

$$V_{in} + V_{C5} = V_{C3} (4)$$

by KCL,

$$i_{C1} = I_{in} - I_{L1} - I_{L2} (5)$$

$$i_{C2} = I_{in} - I_{L3} - I_{L4} (6)$$

$$i_{C3} = I_{in} \tag{7}$$

$$i_{C4} = I_0 \tag{8}$$

$$i_{C5} = I_{in} + I_0 (9)$$

 $i_{C5} = I_{in} + I_0$ (9) During T_{off} period the switches S₁& S₂, diodes D₁ to D₄& D₆ are reverse biased. The capacitors C₄ and C₅ are in a charging condition, while the other capacitors are in a discharge condition. Figure 7 represents the schematic representation of the second mode of operation. Equations 10 to 15 are provided after applying KVL & KCL to obtain the voltage and current expressions of the inductor and capacitor from mode 2 operation in Fig. 6.

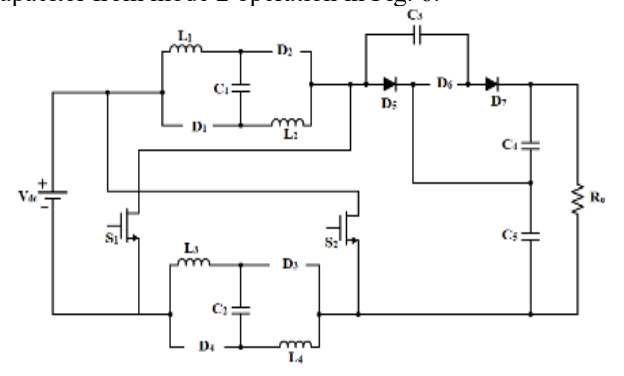


Fig. 6 – Second mode of operation.

By applying KVL and KCL, the equations derived under mode 2 conditions are specified in eq. (10-15), by KVL,

$$V_{in} - 4 V_{L1} + V_{C1} + V_{C3} - V_0 - V_{C2} = 0, (10)$$

$$V_{C5} + V_{C4} = V_0, (11)$$

by KCL,

$$i_{C1} = I_{L1},$$
 (12)

$$i_{C2} = I_{L3},$$
 (13)

$$i_{C3} = i_{C4} = \frac{I_{L2} - I_{L3}}{2},\tag{14}$$

$$i_{C5} = I_0 - I_{L3}. (15)$$

In electronics, gain is an essential concept which is used to control the amount of current or voltage flowing through a circuit. The converter gain is achieved by employing the voltage-second balance condition to eq. (2), (3), (10), and (11). It is expressed in

$$\frac{V_0}{V_{in}} = \frac{7+d}{1-d}. (16)$$

5. STABILITY ANALYSIS OF HGC

The study of power converter characteristics and control strategies is based on modeling approaches. A detailed stability analysis can be found in [16,17]. For system stability analysis, two modes of operation are analyzed and their equations are derived using matrices.

Using the state space equation, the converter's mathematical modeling is investigated, and it is represented

$$\dot{x}(t) = Ax(t) + Bu(t), \tag{17}$$

$$\dot{\mathbf{y}}(t) = C\mathbf{x}(t) + D\mathbf{u}(t). \tag{18}$$

By applying the stability rule the matrix equation can be developed for mode 1 and mode 2, where, $A = A_1d + A_2(1$ d), $B = B_1d + B_2(1-d)$, $C = C_1d + C_2(1-d)$, $D = D_1d + D_2(1-d)$ and d is duty cycle. From mode 1 equation (2-9), the space matrix can be obtained, and from mode 2 operation, the state space matrix can be obtained using equation (10-15). Then the state space analysis obtained from mode 1 and mode 2 are combined and the average state matrix is developed, and it is expressed in eq. (19) and (20).

$$\begin{bmatrix} \vec{l}_{11} \\ \vec{l}_{12} \\ \vec{l}_{13} \\ \vec{l}_{14} \\ \vec{l}_{C1} \\ \vec{l}_{C2} \\ \vec{l}_{C3} \\ \vec{l}_{C4} \\ \vec{l}_{C5} \end{bmatrix} = \begin{bmatrix} 0 & 0 & 0 & 0 & \frac{2(1-d)}{4L_1} & 0 & 0 & 0 & \frac{-(1-d)}{4L_1} \\ 0 & 0 & 0 & 0 & \frac{2(1-d)}{4L_2} & 0 & 0 & 0 & \frac{-(1-d)}{4L_2} \\ 0 & 0 & 0 & 0 & \frac{2(1-d)}{4L_3} & 0 & 0 & 0 & \frac{-(1-d)}{4L_3} \\ 0 & 0 & 0 & 0 & 0 & 0 & 0 & 0 & \frac{-(1-d)}{4L_3} \\ \vec{l}_{C1} \\ \vec{l}_{C2} \\ \vec{l}_{C3} \\ \vec{l}_{C4} \\ \vec{l}_{C5} \end{bmatrix} = \begin{bmatrix} 0 & 0 & 0 & 0 & \frac{2(1-d)}{4L_2} & 0 & 0 & 0 & 0 & \frac{-(1-d)}{4L_2} \\ 0 & 0 & 0 & 0 & 0 & 0 & 0 & 0 & 0 \\ 0 & \frac{1-2d}{2C_3} & 0 & 0 & 0 & 0 & 0 & 0 \\ 0 & \frac{1-2d}{2C_3} & 0 & 0 & 0 & 0 & 0 & 0 \\ 0 & \frac{1-d}{2C_4} & 0 & 0 & 0 & 0 & 0 & \frac{d}{RC_4} & \frac{d}{RC_4} \\ 0 & 0 & 0 & 0 & 0 & 0 & \frac{d}{RC_5} & \frac{d}{RC_5} \end{bmatrix} \begin{bmatrix} I_{11} \\ I_{12} \\ I_{13} \\ I_{14} \\ V_{C2} \\ V_{C3} \\ V_{C4} \\ V_{C5} \end{bmatrix} + \begin{bmatrix} \frac{1+3d}{4L_1} & 0 \\ \frac{1+3d}{4L_2} & 0 \\ \frac{1+3d}{4L_3} & 0 \\ \frac{1+3d}{4L_4} & 0 \\ 0 & \frac{d}{4L_4} \\ 0 & \frac{d}{C_1} \\ 0 & \frac{d}{C_2} \\ 0 & \frac{d}{C_3} \\ 0 & \frac{d}{C_4} \\ 0 & \frac{d}{C_5} \end{bmatrix}$$

$$y = \begin{bmatrix} 0 & 0 & 0 & 0 & 0 & 0 & 1 & 1 \end{bmatrix} \begin{bmatrix} I_{L1} \\ I_{L2} \\ I_{L3} \\ I_{L4} \\ V_{C1} \\ V_{C2} \\ V_{C3} \\ V_{C4} \\ V_{C6} \end{bmatrix}, \tag{20}$$

The transfer function is obtained by applying the R, C & d values to the average space matrix equation. The stability of the converter is then calculated using various techniques, such as the Bode plot, pole-zero maps, root locus graph, and Nyquist plot, to facilitate future system expansion. The stability analysis is verified using the Bode diagram, and the Pole Zero map is represented in Figs. 7 and 8.

558

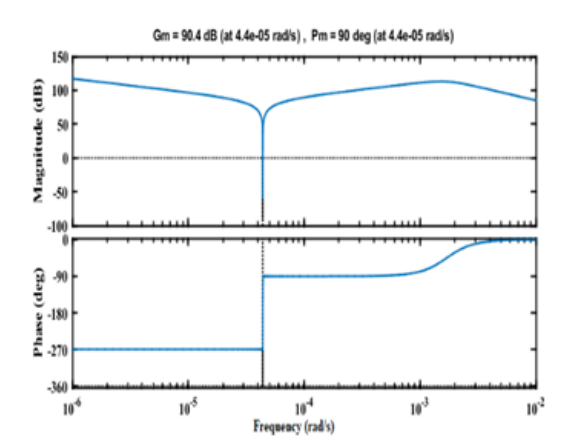


Fig. 7 – Bode Diagram of HGC.

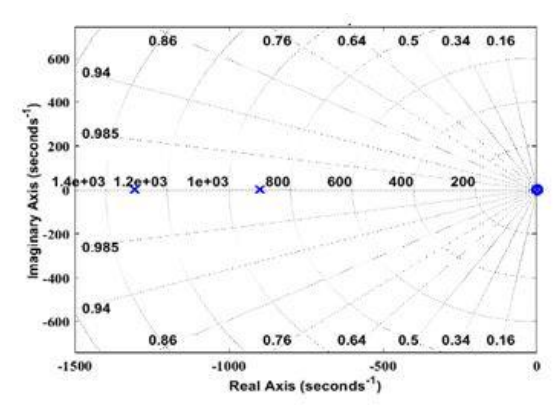


Fig. 8 – Pole Zero map of HGC.

Since the phase margin and gain margin are in a positive range, the system is systematically stable. In the pole-zero map, all the poles and zeros lie on the imaginary axis, indicating that it is also systematically stable. The Nyquist plot of the converter is represented in Fig. 9.

The Nyquist plot is a systematic representation of the system, which depends upon the frequency response under the signal processing unit. The primary purpose of this plot is to analyze the system's stability. Depending upon the transfer function observed using two modes of operation, the plot is generated, and it is observed to be systematically stable.

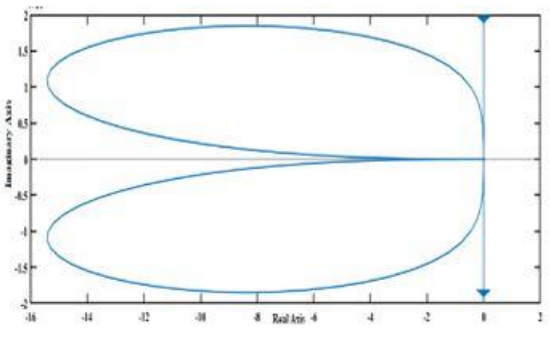


Fig. 9 – Nyquist plot of HGC.

6. SIMULATION RESULTS OF HGC

The function of HGC is validated using a MATLAB-Simulink model [18]. The input source of the system is observed from the PV module, and the output is given to the resistive load. The PV array is designed to produce approximately 250 W, and it is tracked through an MPPT technique using a Simulink model. The maximum power is tracked at a peak point, and its gain is achieved. The Converter is designed for calculating parameter values and is tabulated. The input voltage of 30 V is simulated, and the output is completed at 250 V. Then, the PV Array is interfaced with this Converter module through a DC link capacitor, and its Simulink model is presented. Simulation parameters of the converter are listed in Table 2.

Table 2
Simulation parameters

*	
Parameters	Values
PV Array	250 W
Capacitor C_1, C_2, C_3, C_4, C_5	470 μF
Inductor L_1, L_2, L_3, L_4	330 μΗ
Load Resistor	350 Ω
Source Voltage	30 V
Output Voltage	250 V
Switching Frequency	20 kHz

Interface of PV array and high gain converter is simulated, and it is presented in Fig. 10.

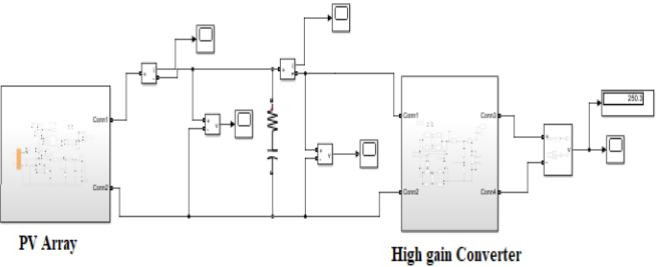


Fig. 10 - Interface of HGC with PV array.

The output voltage, current and power of HGC is simulated using Simulink model and it is presented in Fig. 11.

The interface current and voltages of PV Array and DC-Link capacitor are measured and it is presented in Fig. 12 and Fig. 13.

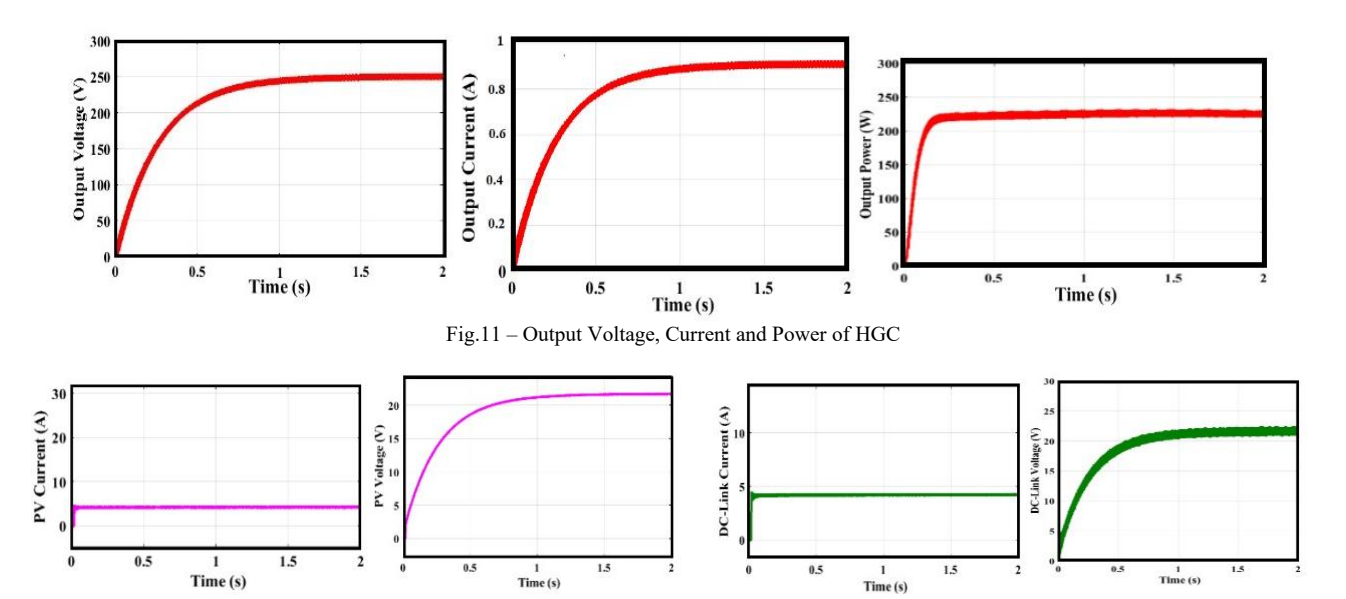


Fig. 12 - Current & Voltage Measurement of PV.

Fig. 13 - Current & Voltage Measurement of DC-Link Capacitor.

The simulation of a high-gain converter, as shown in Fig. 3, is designed for the specified values. Its switching pattern, voltage measurement, and current measurement are simulated and presented. The switching pattern of S_1 and S_2 is the same, and their waveform is presented in Fig. 14.

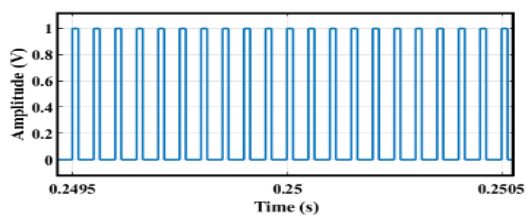


Fig. 14 – Gate pulse of S_1 and S_2 .

The current and voltage measurements of the system are observed using a Simulink model, and they are depicted in Figs. 15 and 16.

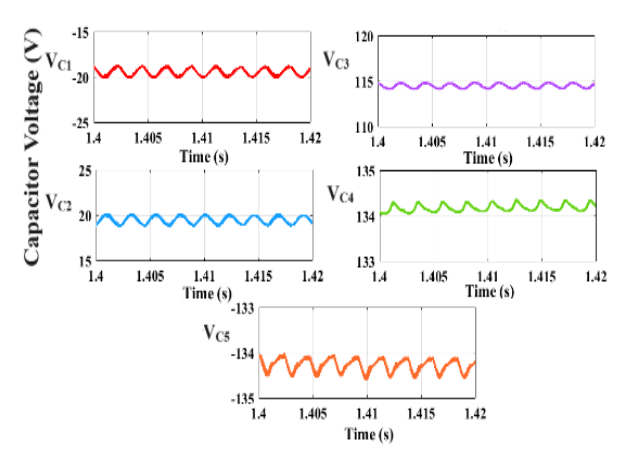


Fig. 15 – Capacitor Voltage Measurement of HGC.

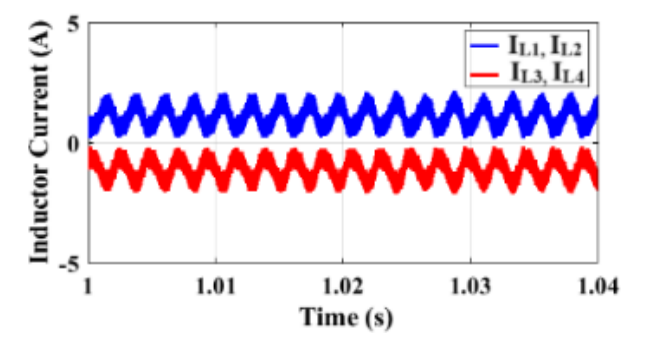


Fig. 16 – Inductor Current Measurement of HGC.

7. ELECTROMAGNETIC SPECTRUM OF HGC

Electromagnetic effects can significantly impact power electronic systems and devices. They might need to be reduced to enable operation free from noise and electromagnetic interference, or they might be the main underlying operating mechanism. Having precise and effective ways and techniques to model these effects is beneficial in both situations. This minimizes costs and the need for additional redesigns by enabling the performance of systems and devices to be anticipated, assessed, and optimized through simulations at an early design stage, before prototyping. According to the EMC Standard, the frequency is measured and observed, as presented in reference [15], and is illustrated in Fig. 17. For high-power converters, the frequency range lies between 10 MHz. In contrast, for low-power applications, it lies between 20 MHz. The outputs obtained by peak and average detectors are compared with the respective limits specified in the CISPR 25 standard. By observing the frequency range, we can predict the further process of the system.

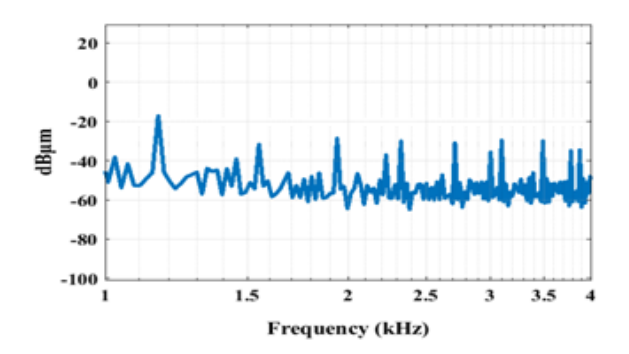


Fig. 17 - Electromagnetic Spectrum of HGC.

8. CONCLUSION

This work focuses on a non-isolated high-gain converter used in renewable energy applications. The power switch in the converter activates simultaneously when the switched cell's inductor continues to receive power from the source voltage. The energy from the inductor will then be transferred to the load if the system is turned off. The VMC of the converter increases the gain of the output voltage. The steady-state analysis, voltage gain, EMC operation, and operating modes are observed. The analysis of the converter is simulated using an open-loop circuit, and the results are presented in a Simulink model, as continuous current is induced, making the HGC suitable for renewable energy applications, such as electric vehicles, uninterruptible power supplies (UPS), and household equipment, as well as DC distribution systems.

CREDIT AUTHORSHIP CONTRIBUTION

- S. Sangeetha: investigation, validation, draft writing.
- R. Ramaprabha: methodology, resources, writing, review, and editing.

Received on 25 January 2024

REFERENCES

- R. Asgarnia, E. Adib, E. Afjei, H. Tarzamni, A novel soft switched SEPIC-based DC-DC converter with high voltage gain, IEEE Open Journal of Power Electronics, 6, pp. 1–9 (2025).
- R. Asgarnia, E. Afjei, A novel high-efficient step-up converter with continuous input current, common ground, and minimum stress on semiconductors, IET Power Electronics (2023).

- M. T. Mathew, Z. Ismail, A four-level interleaved boost converter with a voltage multiplier for high voltage applications, IEEE 8th International Conference on Engineering Technologies and Applied Sciences (ICETAS), Bahrain, pp.1–6 (2023).
- H. Tarzamni, H.S. Gohari, M. Sabahi, J. Kyyra, Nonisolated high stepup DC-DC converters: comparative review and metrics applicability, IEEE Transactions on Power Electronics, 39, 1, pp. 582–625 (2024).
- D. David, N. Ponkumar, N. Salma, S. Dhanalakshmi, S. Baskar, C. Ashok, D. Periyasamy, R. Saravanakumar, A DC-DC boost converter with switching inductor and capacitor with high gain for solar microgrid applications, 2nd International Conference on Recent Trends in Microelectronics, Automation, Computing and Communications Systems (ICMACC), pp. 246–251 (2024).
- A.S. Mansour, M. S. Zaky, A new extended single-switch high gain DC-DC boost converter for renewable energy applications, Scientific Reports, 13, 1 (2023).
- J. Ingilala, I. Vairavasundaram, Investigation of high-gain DC-DC converter for solar PV applications, e-Prime – Advances in Electrical Engineering, Electronics and Energy, 5 (2023).
- H. Li, W. Chen, Y. Zhang, H. Duan, X.F. Cheng, D. Wang, A novel quadratic cascaded coupled inductor high gain DC-DC converter, IEICE Electronics Express (2024).
- R. Thankakan, E.R.S. Nadar, A novel power converter fed by photovoltaic source employing improved incremental conductance algorithm under partial shadow conditions, Rev. Roum. Sci. Techn. – Électrotechn. Et Énerg., 67, 2, pp. 145–150 (2022).
- L. Devarajan, S. Chellathurai, Aquila optimized nonlinear control for DC-DC boost converter with constant power load, Rev. Roum. Sci. Techn. – Électrotechn. Et Énerg., 69, 4, pp. 419–424 (2024).
- H. Sridharan, S. Ramalingam, A. Jawahar, Wide boost ratio in quasiimpedance network converter using switch voltage spike reduction technique, Rev. Roum. Sci. Techn. – Électrotechn. Et Énerg., 68, 3, pp. 259–265 (2023).
- 12. Y. He, L. Chen, X. Sun, An interleaved buck-boost-zeta converter with coupled inductor multiplier cell and zero input current ripple for high step-up application, 12, pp.104807–104817 (2024).
- J. Gnanavadivel, K. Jayanthi, S. Vasundhara, K.V. Swetha, K.J. Keerthana, Analysis and design of high-gain DC-DC converter for renewable energy applications, Automatika (2023).
- A. Ethirajan, R. Ramaprabha, Extended analysis of non-isolated bidirectional high gain converter, Advances in Electrical and Computer Engineering, 23, 4, pp. 89–98 (2023).
- R. Thankakan, E. Rajan, S. Nadar, A novel power converter fed by photovoltaic source employing improved incremental conductance algorithm under partial shadow conditions, Rev. Roum. Sci. Techn. – Électrotechn. Et Énerg., 67, 2, pp. 145–150 (2022).
- S. Lakshmi, R. Ramaprabha, Stability evaluation of four-phase highgain converter by small signal modeling, Rev. Roum. Sci. Techn. – Électrotechn. Et Énerg., 65, pp. 75–80 (2020).
- 17. K.R.S. Vadivu, R. Ramaprabha, Improved steady state and large signal transient response of three-level AC-DC converter using hysteresis modulation-based SMC under DCM, Rev. Roum. Sci. Techn. Électrotechn. Et Énerg., 66, 2, pp. 85–90 (2021).
- 18. www.mathworks.com